Theoretical and Practical Implications of Creep Curve Shape Analyses for 2124 and 2419

H. BURT and B. WILSHIRE

Creep and creep fracture properties are presented for two commercial aluminum alloys, 2124 and 2419, tested at stresses giving creep lives up to about 1000 hours at 373 to 463 K. The results are analyzed using the θ methodology, which quantifies the shape of individual creep curves and the variations in curve shape with changing stress and temperature. The θ relationships are shown to allow reasonable prediction of 100,000-hour stress rupture values, while also explaining the complex creep behavior patterns widely observed with precipitation-hardened alloys.

I. INTRODUCTION

SINCE the 1930s, aluminum alloys have dominated airframe construction for commercial airliners, cargo, and military transport, with the resulting design and production experience ensuring their continuation as the "material of choice" over future decades.[1] However, aluminum has a low melting point ($T_m \sim 933$ K). Hence, creep and creep fracture become important design considerations for airframe components that must operate without failure for long periods under load at temperatures around $0.4T_m$ ($\sim$373 K). For instance, in the European Commission CREEPAL Thematic Network, which began in 1998,[2] the creep life planned for next generation supersonic civil transport was 80,000 flight hours under stresses from 130 to 170 MPa at operational temperatures of 363 to 373 K (maximum 403 K).

Because of the long service lives specified, experimental acquisition of creep design properties for different alloys represents a protracted and expensive task. Only modest reductions in the scale and costs of such long-term programs can then be achieved using standard parametric methods for data extrapolation,[3,4] because these empirical techniques allow estimation of creep lives to just 3 times the longest reliable test results available.[5,6] Moreover, confidence in the validity of the long-term predictions would be enhanced by the availability of extrapolation procedures based on a sound theoretical understanding of the processes controlling strain accumulation and damage evolution during creep.

In the present program, the creep and creep fracture properties of 2419 and 2124 over stress ranges giving creep lives up to about 1000 hours at 373 to 463 K are considered in relation to information derived from studies involving optical and transmission electron microscopy. In addition, the results are analyzed using the θ methodology,[7,8] which seeks to quantify the variations in creep curve shape as the stress and temperature conditions are changed. In this way, an assessment is made of the accuracy with which 100,000-hour stress rupture values[9] can be estimated by analysis of 1000-hour test data, using θ relationships shown to be consistent with the mechanisms governing creep and creep fracture of precipitation-hardened alloys over extended time scales.

H. BURT, Senior Research Officer, and B. WILSHIRE, Professor and EngD/IGDS Director, are with the Materials Research Centre, School of Engineering, University of Wales Swansea, Swansea, SA2 8PP, United Kingdom. Contact e-mail: b.wilshire@swan.ac.uk

Manuscript submitted November 20, 2003.

II. EXPERIMENTAL PROCEDURES

The alloys investigated were 2419-T851 and 2124-T851, having the compositions listed in Table I. These materials were supplied as plates, which were processed as detailed in Table II. X-ray analysis showed no evidence of strong crystallographic textures.

The initial alloy microstructures, as revealed by optical and transmission electron microscopy (Figure 1), can be summarized as follows.

1. 2419-T851 had an average grain diameter of about 0.12 mm, with some large copper-rich particles, which remained undissolved during the solution treatment process. The heat treatment produced a fine dispersion of platelike θ' precipitates ($CuAl_2$).
2. 2124-T851 had an average grain diameter of about 0.15 mm, with some large particles of MnAl and a number of smaller $MnAl_6$ particles. A fine distribution of lath-like S precipitates was observed throughout the grains, with narrow precipitate-free zones at grain boundaries ($<$100-nm wide).

For each alloy, cylindrical testpieces having diameters of 4 mm (with 9.5-mm threaded ends) were machined with 25.4-mm gage lengths normal to the direction of cold stretching (Table II). These specimens were tested in tension using constant true-stress creep machines.[7] The creep properties were studied at 373, 409, 427, 445, and 463 K, with the testpieces heated to the chosen creep temperature in about 3 hours and stabilized at this temperature for 1 hour before applying the load *via* a slow-release jack. High-precision extensometers, incorporating a pair of differential-capacitance transducers, allowed the creep strains to be measured to 10^{-5}. The transducer output was monitored automatically, so that over 500 creep strain/time readings were recorded throughout each test.

Table I. Actual Alloy Compositions (Weight Percent)

Alloy	Cu	Mg	Mn	Ti	Zr	V
2419*	6.06	0.01	0.24	0.09	0.16	0.09
2124*	3.71	1.33	0.49	—	—	—

*2419 and 2124 are high-purity variants of 2219 and 2024, with Fe $<$ 0.1, Si $<$ 0.06, Cr $<$ 0.02, and Zn $\cong$ 0.01.

Table II. Alloy Heat-Treatment Conditions*

Processing Details	2419	2124
Plate thickness (mm)	38	63
Solution treatment temperature (K)	808 ± 4	768 ± 3
Cold stretch (pct)	1.5 to 3.0	1.5
Aging temperature (K)	450	463
Aging time (h)	18	>12

*After solution treatment, the plates were prestrained in tension at room temperature before aging.

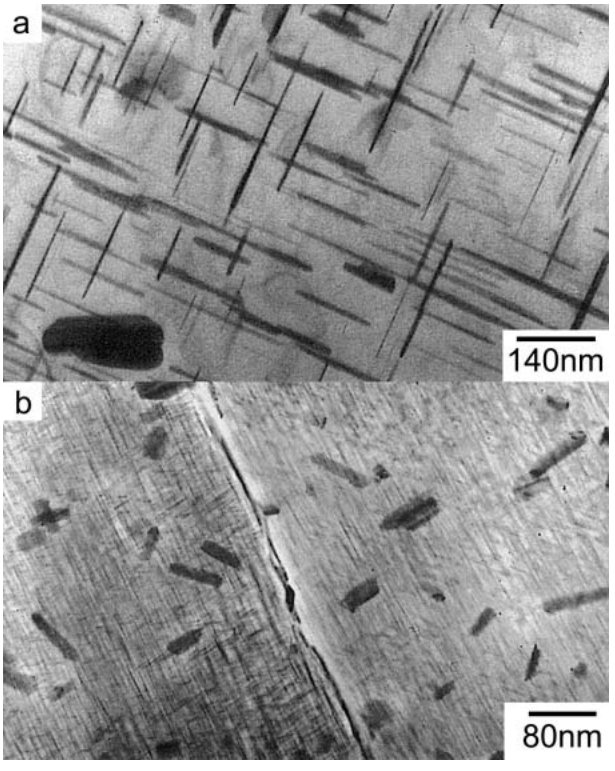

Fig. 1—Transmission electron micrographs showing the precipitate dispersions present before creep exposure of (*a*) 2419 and (*b*) 2124.

III. RESULTS AND DISCUSSION

Under all stress/temperature conditions investigated, normal creep curves were found for both alloys; *i.e.*, after the initial strain on loading, the creep rate decayed during the primary stage, reaching a minimum or secondary value before accelerating in the tertiary stage, which led to failure. When curves of this type are displayed, it has become common practice to describe the observed creep behavior patterns by monitoring only the minimum creep rate ($\dot{\varepsilon}_m$), the time to fracture (t_f), and the total creep strain to failure (ε_f). Hence, this standard procedure is now adopted before progressing to consider the information provided by creep curve shape analyses.

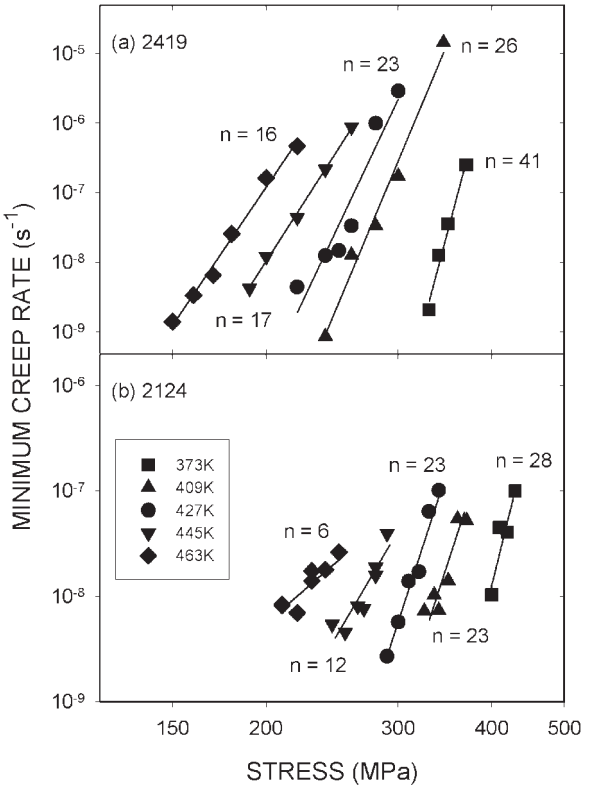

Fig. 2—Stress dependences of the minimum creep rate at 373 to 463 K for (*a*) 2419 and (*b*) 2124.

A. *Power-Law Creep Behavior*

The creep properties of metals and alloys are normally characterized by reference to the dependences of the minimum creep rate on stress (σ) and temperature (T), usually using power-law equations of the form

$$\dot{\varepsilon}_m = A\sigma^n \exp - Q_c/\mathrm{R}T \qquad [1]$$

where the values of A, the stress exponent (n), and the activation energy for creep (Q_c) are widely considered to be constant within defined stress/temperature regimes.

With pure metals, at stresses giving easily measurable creep rates when $T > 0.4T_m$, n usually ranges from about 4 to 6, with Q_c less than or equal to the activation energy for lattice diffusion. In contrast, with particle-hardened alloys, much larger values of n and Q_c are often recorded. Thus, the log $\dot{\varepsilon}_m$/log σ plots in Figure 2 are represented by sets of straight lines to indicate that, as the test temperature increases from 373 to 463 K, n decreases

1. from about 41 to 16 for 2419 (Figure 2(a)) and
2. from about 28 to 6 for 2124 (Figure 2(b)).

Then, because n decreases with increasing temperature, Q_c increases as the applied stress is reduced, with Q_c varying from around 110 to 230 kJmol^{-1} over the stress/temperature

ranges covered. These n and Q_c values indicate that creep is taking place by diffusion-controlled generation and movement of dislocations. Even so, no generally accepted explanation exists to account for the large and variable values of n and Q_c frequently found for alloys strengthened by fine dispersions of precipitates or insoluble particles.[6,10]

B. *Creep Fracture Behavior*

The log $\dot{\varepsilon}_m$/log σ plots in Figure 2 are approximately mirrored by the log t_f/log σ data in Figure 3. This result would be expected because, for many materials,[11]

$$\dot{\varepsilon}_m \cdot t_f = \text{constant} \qquad [2]$$

with the inverse dependence of t_f on $\dot{\varepsilon}_m$ demonstrating that the creep lives are determined by the rates of creep strain accumulation; *i.e.*, creep fracture is strain controlled. However, the gradients of the log t_f/log σ plots ($=-d$ log t_f/d log σ) in Figure 3 do not always correspond with the n values in Figure 2, so that the product $\dot{\varepsilon}_m \cdot t_f$ is not necessarily constant for a given alloy at a fixed creep temperature. Instead, the stress dependences of $\dot{\varepsilon}_m \cdot t_f$ in Figure 4 are broadly consistent with the general patterns of behavior shown in Figure 5 for the creep ductility (ε_f), indicating that

$$\dot{\varepsilon}_m \cdot t_f = X\varepsilon_f \qquad [3]$$

where X is a constant; *i.e.*, Eq. [3] reduces to Eq. [2] when ε_f does not vary significantly with changing stress and temperature.

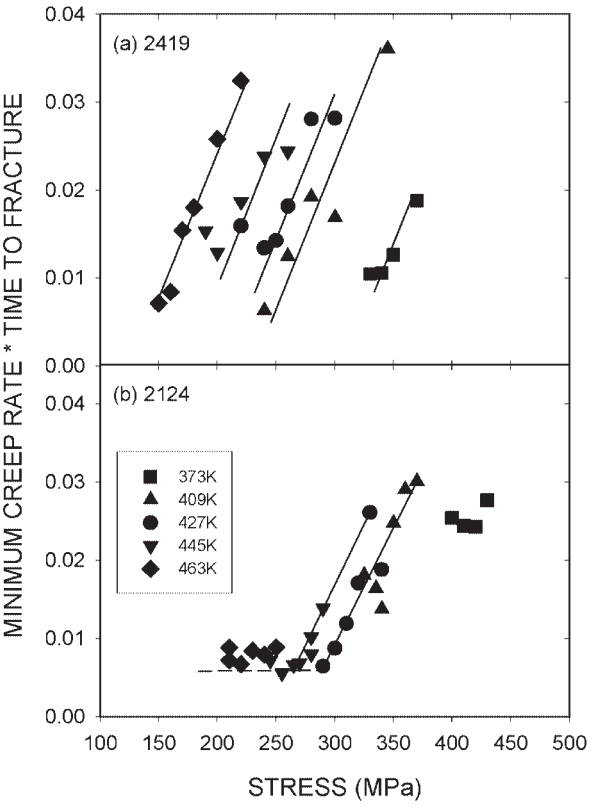

Fig. 4—Stress dependences of the product of the minimum creep rate and the rupture life ($\dot{\varepsilon}_m \cdot t_f$) at 373 to 463 K for (*a*) 2419 and (*b*) 2124.

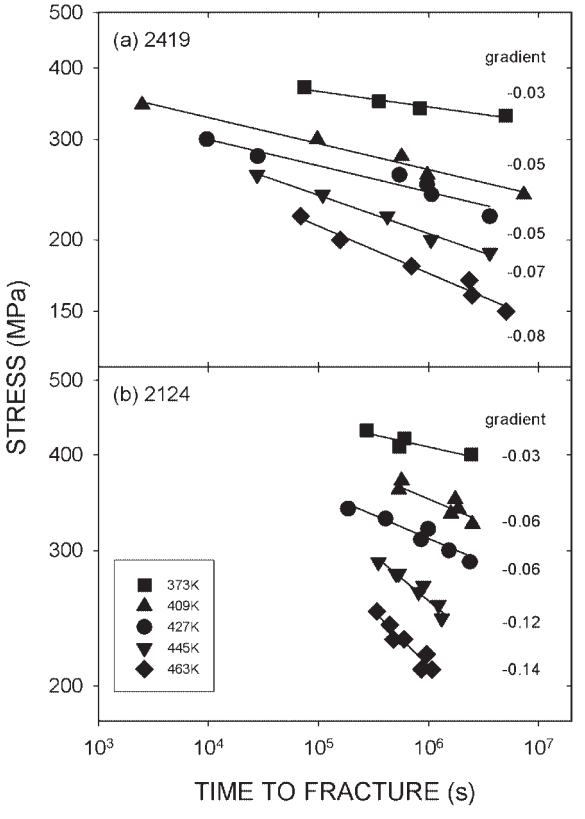

Fig. 3—Stress dependences of the time to failure at 373 to 463 K for (*a*) 2419 and (*b*) 2124.

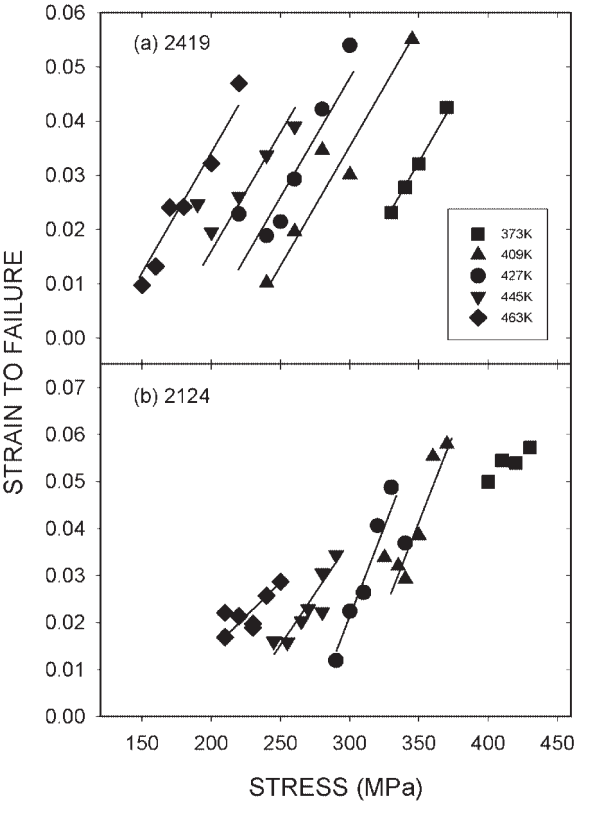

Fig. 5—Stress dependences of the total creep strain to failure at 373 to 463 K for (*a*) 2419 and (*b*) 2124.

Related trends in $\dot{\varepsilon}_m \cdot t_f$ (Figure 4) and ε_f (Figure 5) could be anticipated from the expression defining[12] the creep damage tolerance parameter, λ; namely,

$$\lambda = (\varepsilon_f - \varepsilon_p)/\dot{\varepsilon}_m \cdot t_f \cong \varepsilon_f/\dot{\varepsilon}_m \cdot t_f \quad [4]$$

where $(\varepsilon_f - \varepsilon_p)$ is the tertiary strain, which approximates to ε_f when the primary creep strain (ε_p) is low, giving $X \cong 1/\lambda$ in Eq. [3]. With 2419, $\lambda \cong 1$ to 2.5 at all stress levels studied at 373 to 463 K (Figure 6(a)). Yet, while λ also ranges from 1.5 to 2.5 for 2124 at 373 to 427 K, λ exceeds 2.5 as the test temperature increases toward 463 K (Figure 6(b)).

From Eq. [4], $\lambda \cong 1$ with creep curves characterized by low tertiary strains, with λ then increasing as the tertiary stages become more pronounced. The magnitude of λ should therefore provide an indication of the processes influencing the tertiary acceleration and eventual failure. Indeed, λ values from 1 to 2.5 have been predicted[13] when tertiary creep and fracture are attributable to cavitation, with higher λ values expected when the tertiary stage begins as a consequence of necking (such that $\lambda > 2.5$) or precipitate coarsening (such that $\lambda > 5$). To assess these suggestions, microstructural studies were undertaken in an attempt to clarify the dependences of the λ values on the processes causing tertiary creep under constant true-stress test conditions.

C. *Microstructure Evolution during Creep*

Over the stress/temperature ranges covered for both alloys, failure occurred by nucleation, growth, and linkup of grain-boundary cavities (Figure 7). This observation is compatible with the view[13] that $\lambda \cong 1$ to 2.5 (Figure 6) when cavitation causes the tertiary acceleration and eventual fracture. However, the proposal that $\lambda > 2.5$ when tertiary creep is initiated by the onset of necking[13] cannot explain the occurrence of λ values between 2.5 and 5 at 445 and 463 K for 2124 (Figure 6(b)), because necking was barely discernible under all test conditions considered.

It has been shown that tertiary behavior patterns are markedly affected when the precipitate size and dispersion changes substantially during creep of 7010.[14] To determine the extent to which particle coarsening occurs with 2419 and 2124, thin foils for transmission electron microscopy studies were prepared from specimens tested to failure. Unfortunately, even after creep exposure times of around 1000 hours at 463 K for both alloys, any increases in mean particle diameter were still within foil-to-foil variations for any one sample. Similarly, with a 2124 testpiece strained to 0.008 in 11,360 hours at 427 K, the only discernible feature seemed to be an increase in the width of the particle-free zones at grain boundaries from $<$100 nm to $\sim$200 nm (Figure 8). While this growth of the particle-denuded zones verifies that 2124 is microstructurally unstable during prolonged exposure at 427 K and above, the present studies do not reveal the precise conditions under which particle coarsening begins to affect creep behavior. Alternative approaches therefore must be identified in order to relate the observed variations in λ value (Figure 6) to the process(es) influencing the tertiary acceleration of 2124 and 2419.

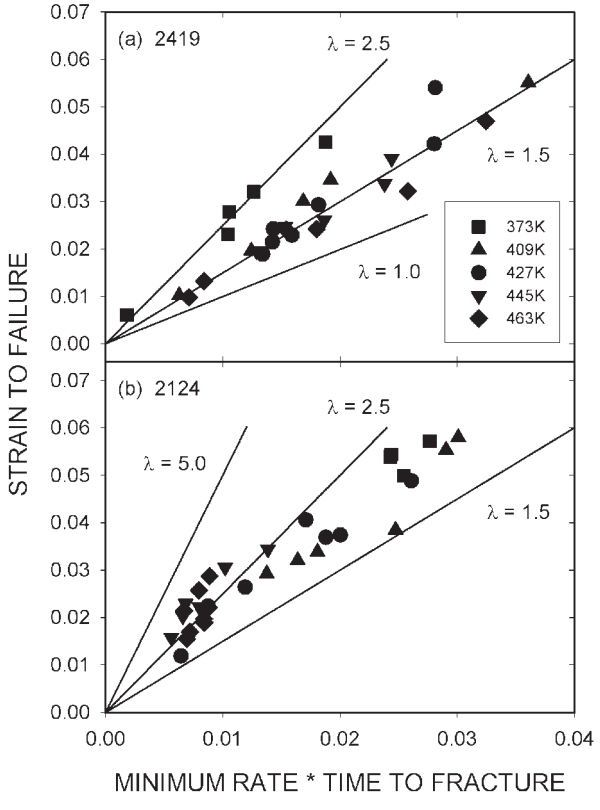

Fig. 6—The relationship between $\dot{\varepsilon}_m \cdot t_f$ and the creep ductility, ε_f, at 373 to 463 K for (*a*) 2419 and (*b*) 2124.

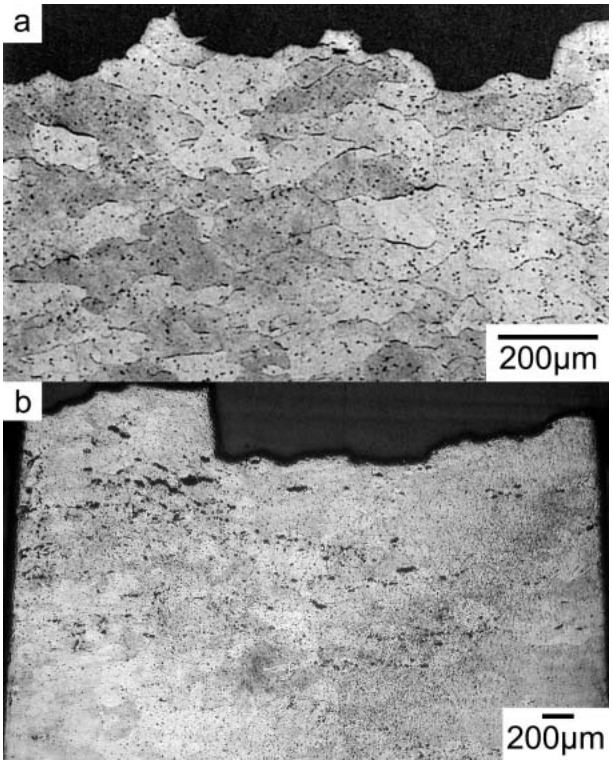

Fig. 7—Appearances of specimens of (*a*) 2419 tested to failure at 200 MPa and 427 K and (*b*) 2124 tested to failure at 330 MPa and 427 K.

D. *Variations in Creep Curve Shape*

Traditional data analysis procedures based largely on $\dot{\varepsilon}_m$, t_f, and ε_f measurements ignore the primary and tertiary stages, which are usually the dominant features of a creep "curve." Yet, the general shapes of normal creep curves can vary for different alloys, with the curve shapes also changing as the test conditions are altered (Figure 9). For example, the creep curves for 2419 show limited tertiary strains over the entire range of stress/temperature conditions investigated (Figure 9(a)), whereas the tertiary stage becomes gradually more pronounced as the stress decreases and the temperature increases for 2124 (Figure 9(b)).

The shape of individual creep curves can also be considered in terms of the variations in creep strain rate ($\dot{\varepsilon}$) with increasing strain (ε) or time (t) throughout the creep life. Adopting this approach, plots of $\dot{\varepsilon}$ as a function of normalized time (t/t_f) reveal that $\dot{\varepsilon}_m$ is a minimum rather than a "secondary" or "steady-state" creep rate, as evident from Figure 10. With the normal creep curves observed for 2419 and 2124, the minimum rate ($\dot{\varepsilon}_m$) must then be reached when the decaying primary rate is offset by the tertiary acceleration associated with "damage processes" such as cavitation, necking, and particle coarsening. Moreover, with the present alloys, the ratio (t_m/t_f) of the time to the minimum rate (t_m) to the time to fracture (t_f) varies distinctively with changing stress and temperature (Figure 11). While $t_m \cong 0.5t_f$ for 2419 at 373 to 463 K, t_m/t_f decreases from ~0.5 at 373 K toward 0.2 or less as the creep temperature approaches 463 K with 2124.

Under the test conditions studied for both alloys, necking can be discounted as the cause of the tertiary stage. For 2419 at all temperatures, when the tertiary stage is not pronounced

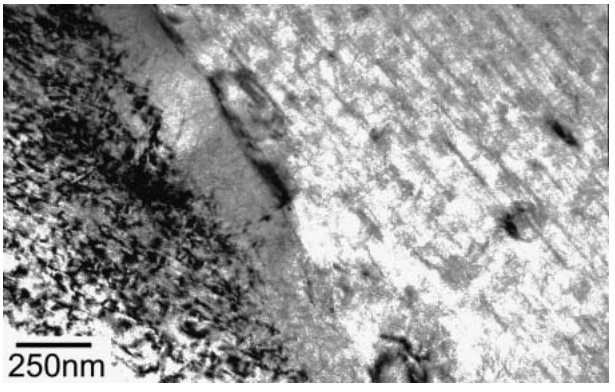

Fig. 8—Transmission electron micrograph showing the precipitate dispersions present in 2124 after a creep exposure of 11,361 h under an applied stress of 220 MPa at 427 K.

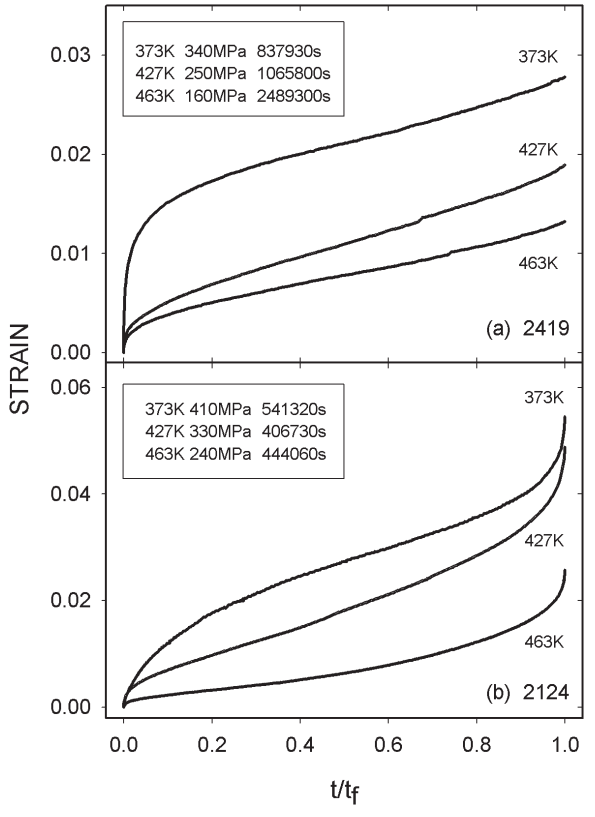

Fig. 9—Creep strain/time curves recorded at 373, 427, and 463 K for (*a*) 2419 and (*b*) 2124.

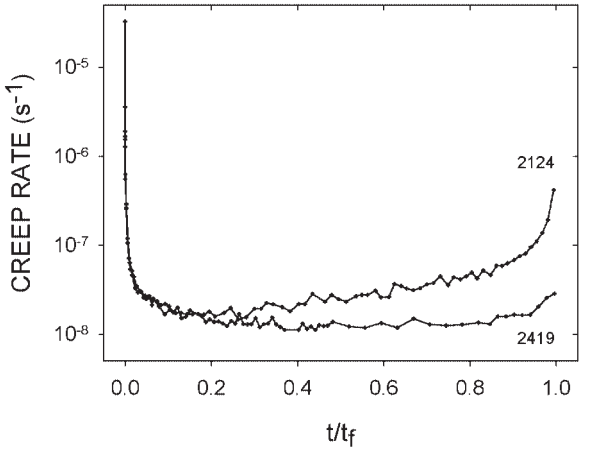

Fig. 10—Variations in the creep strain rate ($\dot{\varepsilon}$) as a function of normalized time (t/t_f) at 427 K for 2419 tested at 240 MPa (when t_f = 107 ks) and for 2124 tested at 320 MPa (when t_f = 93 ks).

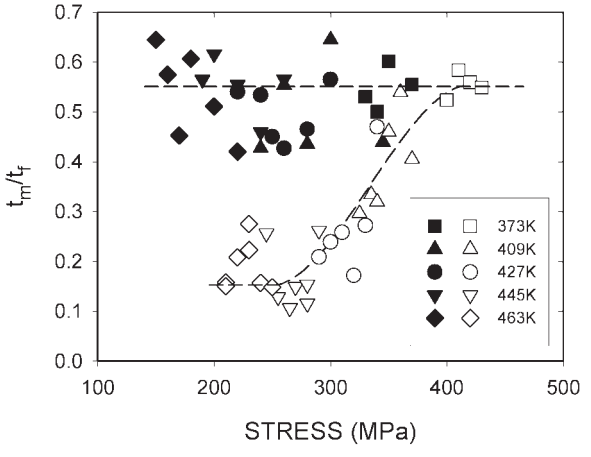

Fig. 11—The stress dependences of the t_m/t_f ratio, where t_m is the time to the minimum creep rate and t_f is the time to fracture, for 2419 (closed symbols) and 2124 (open symbols) at 373 to 463 K.

(Figure 9(a)) so that $t_m \cong 0.5t_f$ (Figure 11) and $\lambda \cong 1$ to 2.5 (Figure 6(a)), it seems that cavitation initiates the tertiary stage and causes eventual failure (Figure 7(a)). However, with decreasing stress and increasing temperature, the tertiary characteristics observed for 2124 differ increasingly from those for 2419. It therefore appears that, with 2124, the principal cause of the onset of tertiary creep changes from cavitation to microstructural instability.

With 2124, even when tertiary creep begins as a result of particle coarsening, cavitation is the cause of failure. Consequently, the tertiary stage becomes more pronounced (Figure 9(b)) as the time for microstructural instability to initiate tertiary creep decreases in relation to the time for cavitation to cause failure, *i.e.*, the t_m/t_f ratio decreases toward 0.2 or less (Figure 11) and the λ value progressively exceeds 2.5 (Figure 6(b)) as the stress is decreased at temperatures approaching 463 K.

When either cavitation or microstructural instability initiates tertiary creep, neck formation late in the tertiary stage will enhance the rate of tertiary acceleration but should have little effect on the t_m/t_f ratio or the λ value. Even so, for materials and test conditions in which necking causes the onset of tertiary creep, usually when large primary strains are accumulated in high stress tests, neck formation will produce a rapid tertiary acceleration; *i.e.*, λ may exceed 2.5, but the comparatively short tertiary duration will mean that $t_m > 0.5t_f$.

On this basis, the present analysis indicates that the relative importance of different tertiary processes can be inferred by inspecting the creep strain/time curves to determine both the λ values and the t_m/t_f ratios.

E. *Analysis of Creep Curve Shapes*

In contrast to conventional "steady-state" approaches, the idea that most normal creep curves should be envisaged in terms of decaying primary and accelerating tertiary stages is an essential feature of the θ Projection Concept.[7,8] Modeling of the dislocation processes controlling strain accumulation and the damage phenomena causing tertiary creep then supports a quantitative description of the variation in creep strain with time as

$$\varepsilon = \theta_1(1 - \exp(-\theta_2 t)) + \theta_3(\exp(\theta_4 t) - 1) \qquad [5]$$

where θ_1 and θ_3 quantify the primary and tertiary strains, while θ_2 and θ_4 are rate parameters governing the curvatures of the primary and tertiary components, respectively.

Using Eq. [5], the accuracy with which the various θ terms can be calculated depends on the extent of the primary and tertiary stages. With 2419 and 2124, θ_1 and θ_2 are determined with less precision when the primary stage becomes less pronounced with decreasing stress (Figure 9). Similarly, the derived θ_3 and θ_4 values become less certain with creep curves displaying little or no tertiary stages. In fact, because the tertiary components are limited with 2419 at 373 to 463 K and with 2124 at 373 K (Figure 9), it proved necessary to analyze the creep curve shapes by adopting a modified form of Eq. [5];[7] namely,

$$\varepsilon = \theta_1(1 - \exp(-\theta_2 t)) + \theta_3\theta_4 t \qquad [6]$$

However, with Eq. [6], only the product $\theta_3\theta_4$, not the individual values of θ_3 and θ_4, can be derived.

Nonlinear least-squares curve-fitting routines are available[7] to evaluate θ_i (where $i = 1, 2, 3$, or 4), with the derived θ values representing each creep curve accurately over most of the creep life. Moreover, the systematic variations in curve shape (Figure 9) can be quantified[8] through plots of log θ_i against (σ/σ_y), where σ_y is the high-strain-rate yield stress at the creep temperature (Figures 12 through 15). In the T851 condition, σ_y is known to decrease from ~421 to 357 MPa with 2124 and from ~327 to 222 MPa with 2219 (equivalent to 2419, Table I) as the test temperature increases from 373 to 463 K.[9] On this basis, when the creep curves for 2124 at 409 to 463 K are described by Eq. [5],

$$\theta_1 = G_1 \exp H_1(\sigma/\sigma_y) \qquad [7a]$$

$$\theta_2 = G_2 \exp -(Q_2 - H_2[\sigma/\sigma_y])/RT \qquad [7b]$$

$$\theta_3 = G_3 \exp H_3(\sigma/\sigma_y) \qquad [7c]$$

$$\theta_4 = G_4 \exp -(Q_4 - H_4[\sigma/\sigma_y])/RT \qquad [7d]$$

where G_i and H_i are constants, while Q_2 and Q_4 are the activation energies associated with θ_2 and θ_4, respectively. Thus, θ_1 in Figure 12(b) and θ_3 in Figure 14(a) decrease with decreasing stress, approaching low stress plateau values of ~0.002 for θ_1 and ~0.001 for θ_3; *i.e.*, the strainlike parameters (θ_1 and θ_3) are characterized by temperature dependences comparable with that for σ_y. The sets of near-parallel straight-line log $\theta_2/(\sigma/\sigma_y)$ and log $\theta_4/(\sigma/\sigma_y)$ plots at different temperatures are then superimposed onto single lines (Figures 13(b) and 14(b)) by temperature compensation through Arrhenius terms with $Q_2 \cong Q_4 \cong 145$ kJmol^{-1}; *i.e.*, activation energies close to that expected for lattice diffusion in the alloy matrix.

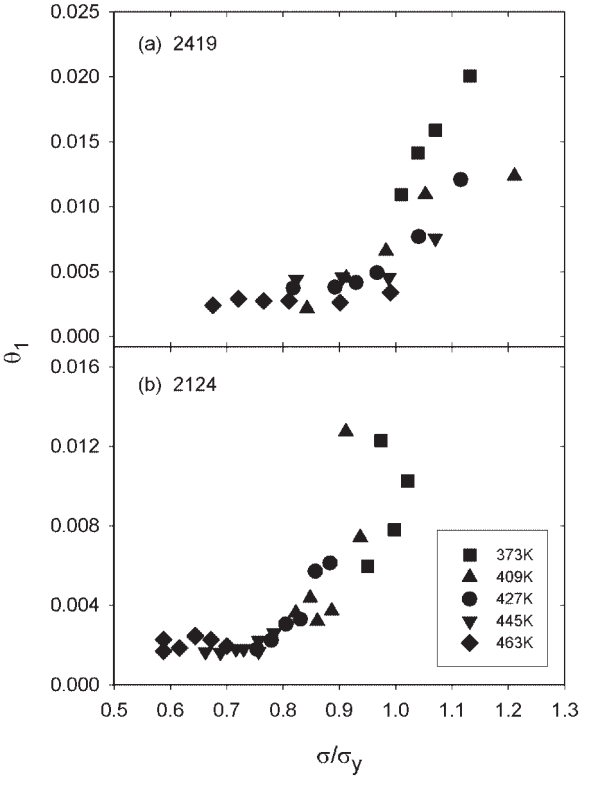

Fig. 12—The stress dependences of the primary parameter, θ_1, at 373 to 463 K for (*a*) 2419 and (*b*) 2124.

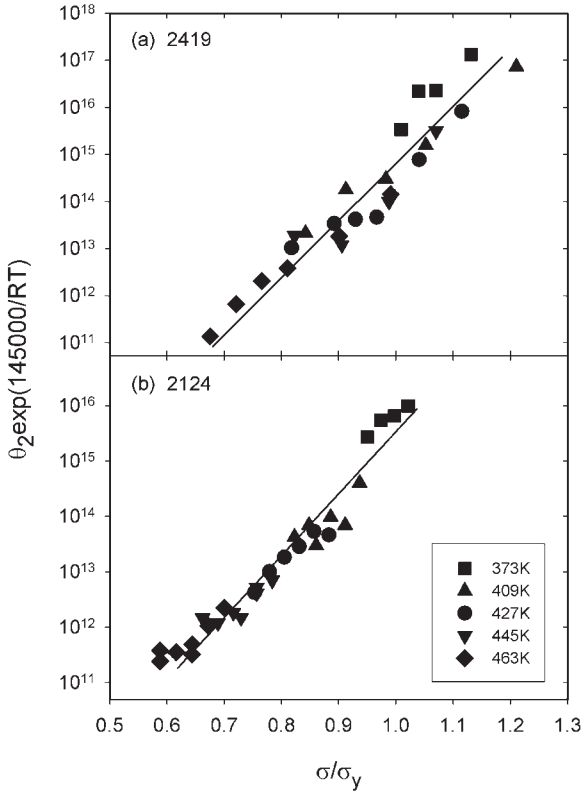

Fig. 13—The stress dependences of the primary rate parameter, θ_2, at 373 to 463 K for (*a*) 2419 and (*b*) 2124.

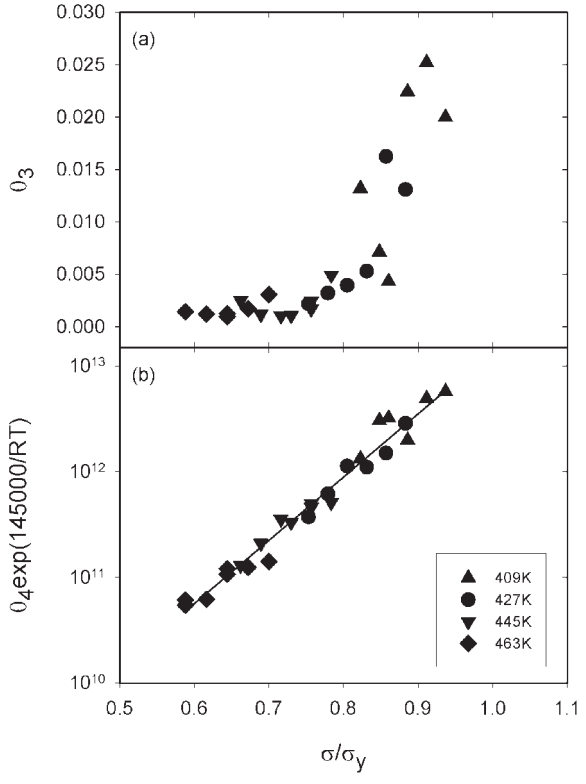

Fig. 14—The stress dependences of (*a*) θ_3 and (*b*) θ_4 for 2124 at 409 to 463 K.

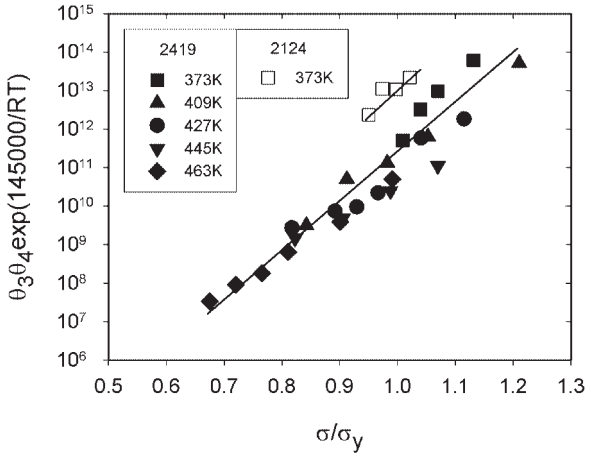

Fig. 15—The stress dependences of the tertiary product, $\theta_3\theta_4$, for 2419 at 373 to 463 K and for 2124 at 373 K.

Using Eq. [6] to describe the creep curves recorded for 2419 at 373 to 463 K and for 2124 at 373 K, the derived θ_1 and θ_2 values are again well represented by Eqs. [7a] and [7b], with $Q_2 \cong 145$ kJmol^{-1} (Figures 12 and 13). The temperature dependence of the tertiary product ($\theta_3\theta_4$) is then governed largely by the rate parameter, θ_4. Hence, the near-parallel straight-line log $\theta_3 \cdot \theta_4/(\sigma/\sigma_y)$ plots at each temperature for 2419 can also be rationalized using an activation energy of ~145 kJmol^{-1} (Figure 15).

The θ relationships are fully consistent with the processes governing the primary and tertiary behavior of 2419 and 2124. Creep occurs by diffusion-controlled generation and movement of dislocations in the alloy matrices, so $Q_2 \cong 145$ kJmol^{-1} (Figure 13). Similarly, the fact that an activation energy of ~145 kJmol^{-1} rationalizes the θ_4 values for 2124 (Figure 14(b)) and the $\theta_3\theta_4$ data for 2419 (Figure 15) is compatible with the dominant tertiary process being either strain-controlled cavitation or particle coarsening. These straightforward outcomes of the θ analyses then contrast strongly with the problems of explaining[10] the large and variable n and Q_c values recorded for particle-strengthened alloys when the stress and temperature dependences of $\dot{\varepsilon}_m$ are described using power-law relationships (Figure 2).

F. *Strain Rate Variations during Creep*

Once the relevant θ values are determined for a series of creep curves, the θ methodology also introduces a novel way of quantifying and interpreting the changes in creep strain rate ($\dot{\varepsilon}$) throughout the creep life (Figure 10). Consider first the determination of $\dot{\varepsilon}_m$.

When creep curves exhibiting only limited tertiary stages are described by Eq. [6],

$$\dot{\varepsilon} = \theta_1\theta_2 \exp(-\theta_2 t) + \theta_3\theta_4 \qquad [8]$$

with $\theta_3\theta_4 \cong \dot{\varepsilon}_m$, as shown in Figure 16 for 2419 at 373 to 463 K and for 2124 at 373 K. In contrast, with normal curves displaying well-defined primary and tertiary stages, Eq. [5] gives

$$\dot{\varepsilon} = \theta_1\theta_2 \exp(-\theta_2 t) + \theta_3\theta_4 \exp(\theta_4 t) \qquad [9]$$

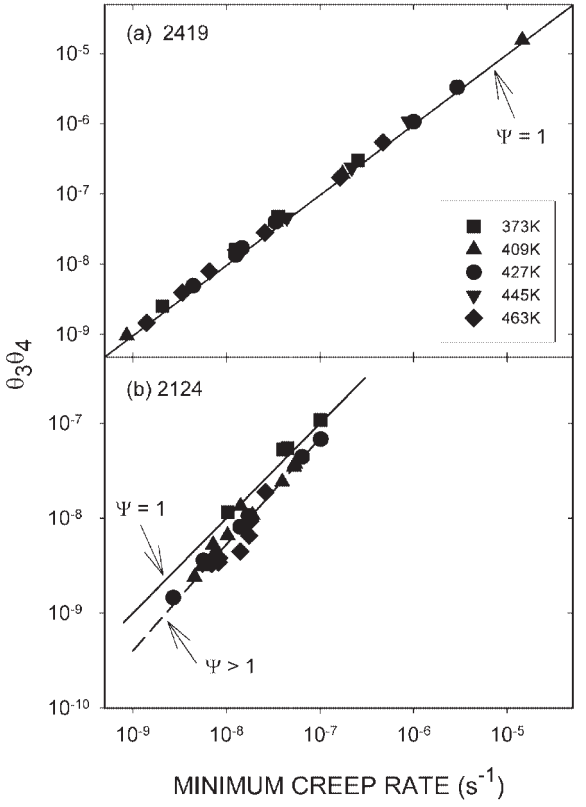

Fig. 16—The relationships between the minimum creep rate, $\dot{\varepsilon}_m$, and the tertiary product, $\theta_3\theta_4$, at 373 to 463 K for (*a*) 2419 and (*b*) 2124.

The minimum rate is then reached after a time, t_m, where

$$t_m = [1/(\theta_2 + \theta_4)] \ln (\theta_1\theta_2^2/\theta_3\theta_4^2) \quad [10]$$

allowing $\dot{\varepsilon}_m$ to be calculated by substituting the derived t_m value into Eq. [9]. For 2124 at 409 to 463 K, the $\dot{\varepsilon}_m$ values computed in this way exactly matches the measured rates in Figure 2. For all curves obtained for 2419 and 2124, the correct values of $\dot{\varepsilon}_m$ are therefore predicted, irrespective of whether Eq. [8] or [9] is used. However, defining $\dot{\varepsilon}_m$ as

$$\dot{\varepsilon}_m = \Psi\theta_3\theta_4 \quad [11]$$

$\Psi = 1$ for 2419 at 373 to 463 K, whereas Ψ increases toward 2 or more as the applied stress decreases at temperatures approaching 463 K with 2124 (Figure 16). Using the θ relationships illustrated schematically in Figure 17, these Ψ values allow calculation of the changes in creep rate ($\dot{\varepsilon}$) as t increases, initially from $t = 0$ to $t = t_m$ and then from $t = t_m$ to $t = t_f$.

When $t = 0$, Eqs. [8] and [9] give the calculated initial creep rate ($\dot{\varepsilon}_o$) as

$$\dot{\varepsilon}_o = \theta_1\theta_2 + \theta_3\theta_4 \quad [12]$$

where $\theta_1\theta_2$ is the initial "primary" rate and $\theta_3\theta_4$ is the initial "tertiary" rate. The results for 2419 and 2124 in Figure 18 then demonstrate that $\dot{\varepsilon}_o$ is governed largely by $\theta_1\theta_2$, *i.e.*, $\theta_1\theta_2 \gg \theta_3\theta_4$. This high initial rate* decays continuously

*As evident from Fig. 10, the actual initial creep rates are substantially larger than the calculated values (Eq. [12]), because the θ equations do not fit the measured creep strain/time curves during brief periods immediately after the initial strains on loading, *i.e.*, when t is less than about $0.1t_m$.[15]

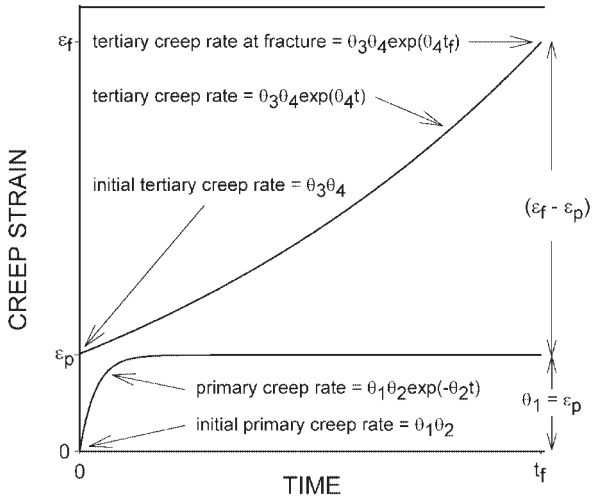

Fig. 17—Schematic representation of the physical significance of various θ relationships. The magnitudes of the θ parameters govern the changes in creep strain and creep rate with increasing time, quantifying the shape and extent of the primary and tertiary stages.

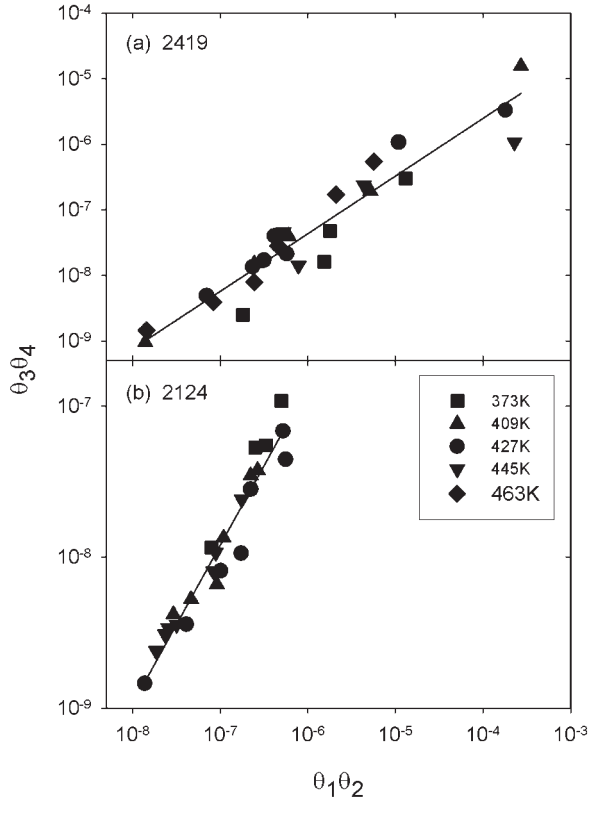

Fig. 18—The relationships between $\theta_1\theta_2$ and $\theta_3\theta_4$ at 373 to 463 K for (*a*) 2419 and (*b*) 2124.

with time (*i.e.*, $\theta_1\theta_2 \exp(-\theta_2 t)$ decreases toward zero as $t \rightarrow t_m$), eventually reaching the minimum rate ($\dot{\varepsilon}_m$). Hence, $\dot{\varepsilon}_m \cong \theta_3\theta_4$ when the rate of cavitation-induced tertiary acceleration is low, whereas $\dot{\varepsilon}_m > \theta_3\theta_4$ when microstructural instability accelerates the initial tertiary rate ($\theta_3\theta_4$) over the period from $t = 0$ to $t = t_m$ (Figure 16).

In a similar manner, the dominant damage mechanism governs the creep rate acceleration as t increases from t_m to t_f.

Combining Eq. [9] with Eq. [11], the ratio of the calculated creep rate at fracture ($\dot{\varepsilon}_f$) to the minimum creep rate ($\dot{\varepsilon}_m$) is given by

$$\dot{\varepsilon}_f/\dot{\varepsilon}_m = \exp(\theta_4 t_f)/\Psi \quad [13]$$

with the relationships between θ_4 and t_f shown for 2124 at 409 to 463 K in Figure 19. Furthermore, the values of Ψ (Figure 16) and $\theta_4 t_f$ (Figure 19) determine not only the $\dot{\varepsilon}_f/\dot{\varepsilon}_m$ ratio (Eq. 13) but also the λ value (Eq. 4); *i.e.*, from Eq. [5] when $t = t_f$,

$$(\varepsilon_f - \varepsilon_p) = \theta_3(\exp(\theta_4 t_f) - 1) \quad [14]$$

with $\varepsilon_p \cong \theta_1$ (Figure 17). By substituting for $\dot{\varepsilon}_m$ using Eq. [11] and for $(\varepsilon_f - \varepsilon_p)$ using Eq. [14], the expression for λ (Eq. [4]) becomes

$$\lambda = [\exp(\theta_4 t_f) - 1]/\Psi\theta_4 t_f \quad [15]$$

With 2124 at 409 K, $\Psi \cong 1$ (Figure 16(b)) and $\theta_4 t_f \cong 1$ (Figure 19), with comparable values of Ψ and $\theta_4 t_f$ expected for 2124 at 373 K and for 2419 at 373 to 463 K when only limited tertiary stages are also observed (Figure 9). Equation [15] then confirms that $\lambda \cong 1$ to 2.5 when cavitation causes tertiary creep and fracture, with the tertiary acceleration being low as t increases from t_m to t_f, so the creep rate increases only from $\dot{\varepsilon}_m$ to about 3 $\dot{\varepsilon}_m$ ($=\dot{\varepsilon}_f$ in Eq. [13]). In contrast, as the test duration increases at temperatures approaching 463 K with 2124, $\Psi \rightarrow 2$ or more (Figure 16(b)) and $\theta_4 t_f \rightarrow 3$ (Figure 19). When the cause of the tertiary acceleration changes from cavitation to microstructural instability, Eq. [15] shows that $\lambda > 2.5$, with the tertiary stage becoming more pronounced as the $\dot{\varepsilon}_f/\dot{\varepsilon}_m$ ratio increases to 10 or more (Eq. [13]). In this way, the θ relationships offer a quantitative description and a rational mechanistic interpretation of the changes in creep rate throughout the creep life, simultaneously accounting for the λ variations recorded for 2419 and 2124 (Figure 6).

G. *Prediction of Long-Term Creep Lives*

In addition to explaining changes in creep curve shape, the present data sets also permit an assessment to be made of the accuracy with which θ analyses of the systematic variations in the shapes of short-term creep curves allow prediction of long-term property values.

The stresses required to cause fracture in times up to 100,000 hours have been determined experimentally for 2124 at 373 to 478 K.[9] This information is shown in Figure 20, together with the stress rupture values now found for 2124 at 373 to 463 K (Figure 3(b)). Similarly, independent measurements have been made to indicate the stresses causing failure of 2219 in times up to 100,000 hours at 423, 448, and 478 K, but only for times up to 1000 hours at 373 K.[9] These results are compared in Figure 21 with the present stress rupture data for 2419 at 373 to 463 K (Figure 3(a)). Clearly, the behavior patterns reported for 2219 are fully consistent with the current observations for the high-purity variant, 2419 (Table I), so the results for 2219 can provide a check on the long-term creep lives predicted for 2419.

With normal creep curves, which allow the θ parameters in Eq. [5] to be determined at a specified stress and

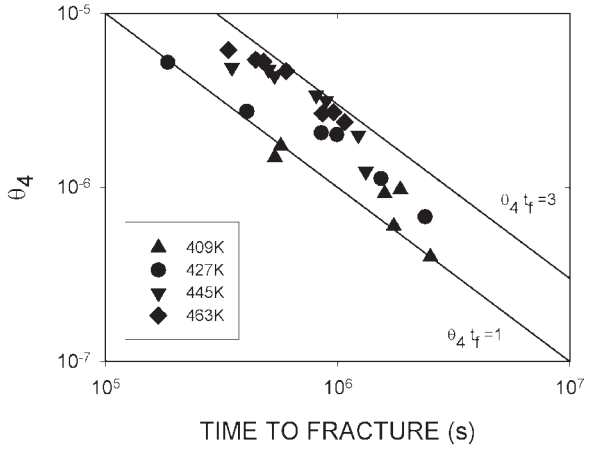

Fig. 19—The dependence of the creep rupture life, t_f, on the tertiary rate parameter, θ_4, at 409 to 463 K for 2124.

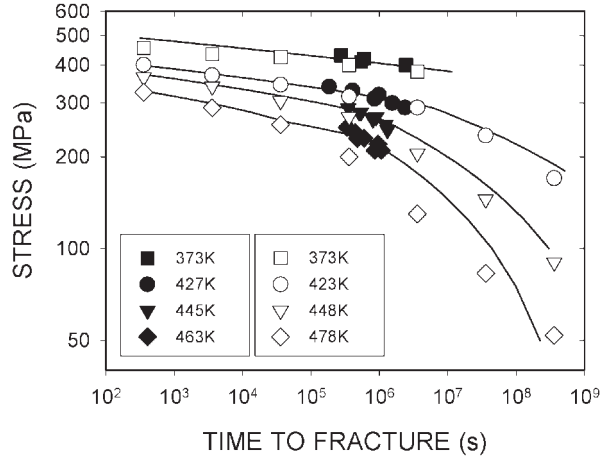

Fig. 20—The stress dependences of the creep lives predicted by θ analysis (solid lines) of the short-term data obtained for 2124 at 373 to 463 K (closed symbols), together with measured long-term data[9] at 373 to 478 K (open symbols).

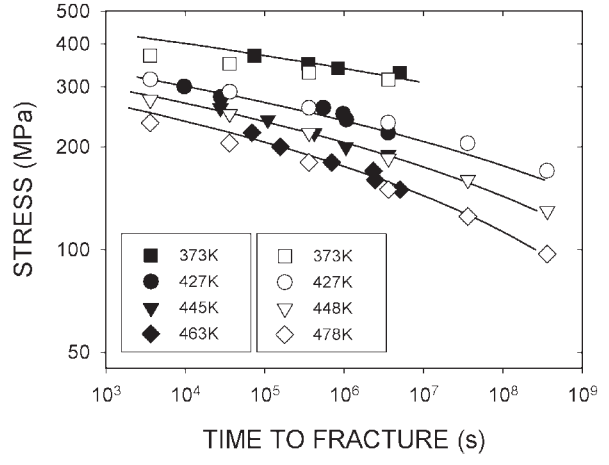

Fig. 21—The stress dependences of the creep lives predicted by θ analysis (solid lines) of the short-term data obtained for 2419 at 373 to 463 K (closed symbols), together with experimental data[9] at 373, 423, 448, and 478 K for 2219 (open symbols).

temperature, the creep life can be computed by solving the equation

$$\theta_1(1 - \exp(-\theta_2 t)) + \theta_3(\exp(\theta_4 t) - 1) - \varepsilon_f = 0 \quad [16]$$

for $t = t_f$.[7,8] However, this method of predicting long-term creep lives is complicated by the difficulty of estimating low-stress ε_f values reliably when the creep ductility falls rapidly with decreasing stress in short-term tests (Figure 5). Moreover, Eq. [16] cannot be used with creep curves described by Eq. [6], which gives $\theta_3\theta_4$ not separate θ_3 and θ_4 values. An alternative extrapolation procedure based on $\theta_3\theta_4$ determinations therefore must be employed.

Using Eq. [6] to quantify the curves recorded for 2419, $\theta_3\theta_4 \cong \dot{\varepsilon}_m$ (Figure 16(a)), so linear extrapolation of the log $\theta_3\theta_4$/stress relationships (Figure 15) gives the log $\dot{\varepsilon}_m$/log σ predictions in Figure 22(a). Long-term t_f estimates are then obtained by projecting the log $\dot{\varepsilon}_m$/log t_f results in Figure 23, demonstrating an impressive fit with the experimentally determined stress-rupture properties for 2219 (Figure 21). For 2124, $\dot{\varepsilon}_m$ (Figure 22(b)) and t_f estimates (Figure 20) were derived using comparable procedures, but with $\dot{\varepsilon}_m > \theta_3\theta_4$ above 427 K (Figure 16(b)) and with low-stress plateau values of 0.001 for θ_3 (Figure 14(a)) and 0.006 for $\dot{\varepsilon}_m \cdot t_f$ (Figure 4). Clearly, the predicted long-term t_f values are again in good agreement with the measured stress-rupture data shown for 2124 in Figure 20.

H. *Prediction of Power-Law Creep Behavior*

The t_f estimates obtained by θ analyses of creep curves having maximum lives of about 1000 hours fit well with the independently measured 100,000 stress rupture properties (Figures 20 and 21). Hence, equivalent predictive accuracy should be achieved when the same θ relationships are used to compute $\dot{\varepsilon}_m$ values over comparable stress/temperature ranges (Figure 22). Although experimental long-term $\dot{\varepsilon}_m$ values are not available to check the predictions in Figure 22, the trends in the log $\dot{\varepsilon}_m$/log σ data obviously match those for the measured and predicted log t_f/log σ relationships in Figures 20 and 21. This would be expected because the creep lives are determined by the rates of creep strain accumulation. As with the log t_f/log σ behavior, the predicted log $\dot{\varepsilon}_m$/log σ plots curve gradually with changing applied stress; *i.e., n* increases progressively from low values at low stresses to very high values as the stress is raised toward the ultimate tensile strength at the creep temperature. This gradual curvature contradicts the common assumption that log $\dot{\varepsilon}_m$/log σ data for particle-strengthened alloys should be represented by successive regimes with $n \cong 1$, $n \cong 4$, and $n > 4$ as the dominant creep mechanism changes with increasing stress.

If different mechanisms controlled the creep properties (and therefore the creep fracture characteristics) within different stress/temperature regimes, analyzing data collected in one mechanism regime could not predict the behavior patterns displayed in another regime. The fact that θ analyses of short-term data allow long-term property values to be estimated with reasonable accuracy then indicates that essentially the same dislocation processes are operative, irrespective of the n value recorded.[6] Indeed, it is apparent from the projected log $\dot{\varepsilon}_m$/log σ curve sets in Figure 22 that the varying n values observed for the present alloys (Figure 2) are merely a consequence of tests at different temperatures being conducted over narrow stress ranges giving easily measurable strain rates ($\sim 10^{-9}$ to 10^{-5} s^{-1}).

When creep takes place by diffusion-controlled generation and movement of dislocations, the primary creep rate decreases as the dislocation density increases with increasing creep strain. With normal creep curves, the minimum rate ($\dot{\varepsilon}_m$) then occurs when the decaying primary creep rate is offset by the tertiary acceleration caused by "damage processes" such as cavitation, microstructural instability, and

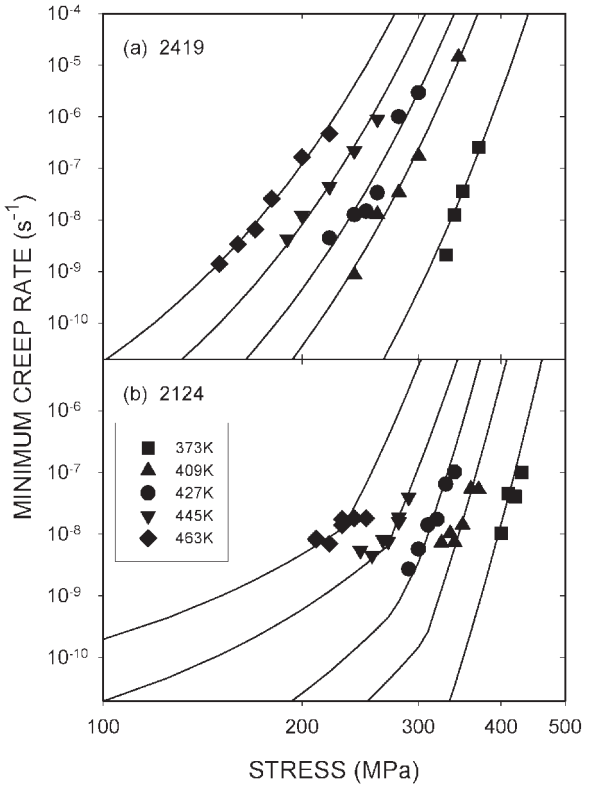

Fig. 22—Stress/minimum creep rate relationships predicted by θ analysis of the short-term data obtained at 373 to 463 K for (*a*) 2419 and (*b*) 2124.

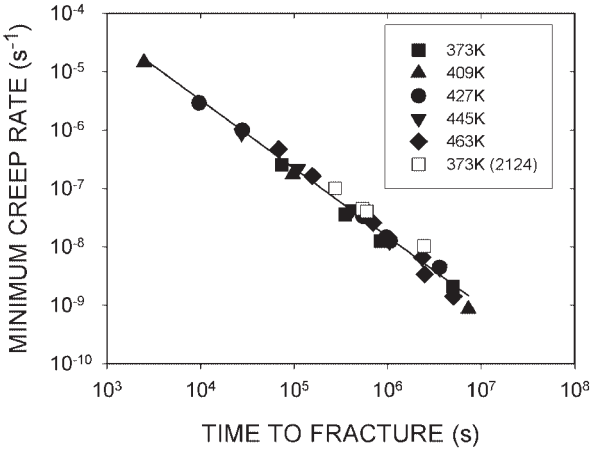

Fig. 23—The dependences of the creep life (t_f) on the minimum creep rate ($\dot{\varepsilon}_m$) for 2419 at 373 to 463 K and for 2124 at 373 K.

neck formation. The primary strain levels and the relative importance of the various tertiary phenomena differ for different materials and test conditions, resulting in systematic changes in creep curve shape, which can be quantified through the θ relationships. The present analysis therefore supports the view[7,8] that changes in n and Q_c (Eq. [1]) are a consequence not of changes in the dominant creep mechanism but of the complex dependence of $\dot{\varepsilon}_m$ on the variations in curve shape that occur with changing stress and temperature.

IV. CONCLUSIONS

Creep property sets obtained for 2124 and 2419 at 373 to 463 K have been analyzed by extending standard approaches for creep data representation to include the θ methodology for quantification of creep curve shapes.

The θ relationships allow identification of the deformation and damage processes causing the creep curve shape to vary systematically with changing stress and temperature. Moreover, the large and variable values of n and Q_c found when power-law equations are used to describe the creep properties of precipitation-hardened alloys are attributable not to changes in the dominant creep mechanisms but to the complex dependence of the minimum creep rate on the changing creep curve shape. In addition, independently measured 100,000-hour stress rupture values can be predicted with reasonable accuracy by θ analyses of the systematic shape variations of creep curves recorded in tests lasting up to about 1000 hours, *i.e.*, an extrapolation of two orders of magnitude in time compared with the threefold maximum extrapolation achieved with traditional parametric methods.

REFERENCES

1. J.C. Williams and E.A. Starke, Jr.: *Acta Mater.*, 2003, vol. 51, pp. 5775-99.
2. Y. Girard, J.C. Ehrström, and J.H. Rantala: in *Creep Deformation—Fundamentals and Applications*, R.S. Mishra, J.C. Earthman, and S.J. Raj, eds., TMS, Warrendale, PA, 2002, pp. 409-19.
3. F.R. Larson and J. Miller: *Trans. ASME*, 1952, vol. 74, pp. 765-775.
4. R.L. Orr, O.D. Sherby, and J.E. Dorn: *Trans. ASM*, 1954, vol. 46, pp. 113-28.
5. R.F. Johnson and J. Glen: *Proc. Conf. on Creep Strength of Steels and High Temperature Alloys*, The Metals Society, London, 1973, pp. 34-42.
6. B. Wilshire: *Metall. Mater. Trans. A*; 2002, vol. 33A, pp. 241-48.
7. R.W. Evans and B. Wilshire: *Creep of Metals and Alloys*, The Institute of Metals, London, 1985.
8. R.W. Evans and B. Wilshire: *Introduction to Creep*, The Institute of Materials, London, 1993.
9. H. Baker *et al.: Metals Handbook*, Ninth Edition vol. 2, ASM, Metals Park, OH, 1979.
10. E. Arzt: *Res. Mech.*, 1991, vol. 31, pp. 399-453.
11. F.C. Monkman and N.J. Grant: *Proc. ASTM*, 1956, vol. 56, pp. 593-605.
12. F.A. Leckie and D.R. Hayhurst: *Acta Metall.*, 1977, vol. 25, pp. 1059-70.
13. M.F. Ashby and B.F. Dyson: in *Advances in Fracture Research*, S.R. Valluri, ed., Pergamon Press, Oxford, United Kingdom, 1984, vol. 1, pp. 3-30.
14. B. Wilshire and H. Burt: *Mater. Sci. Forum*, 2002, vols. 396–402, pp. 1309-14.
15. W.J. Evans and B. Wilshire: *Trans. TMS-AIME*, 1968, vol. 242, pp. 1303-07.